JACS Au
AN OPEN ACCESS JOURNAL OF THE AMERICAN CHEMICAL SOCIETY

pubs.acs.org/jacsau
Article

Epigenetic Modifier Drug Valproic Acid Enhances Cancer Metaphase Chromosome Elasticity and Electron Transport: An Atomic Force Microscopy Approach

Tanya Agrawal, Debashish Paul, Amita Mishra, Ganesan Arunkumar, and Tatini Rakshit*

Cite This: JACS Au 2025, 5, 766−778
Read Online

ACCESS | Metrics & More | Article Recommendations | Supporting Information

ABSTRACT: The structural integrity of the chromosomes is essential to every functional process within eukaryotic nuclei. Chromosomes are DNA-histone complexes that are essential for the inheritance of genetic information to the offspring, and any defect in them is linked to mitotic errors, cancer growth, and cellular aging. Changes in the mechanical properties of a chromosome could lead to its compromised function and stability, leading to chromosome breaks. Here, we studied the changes in chromosome physical properties using metaphase chromosomes isolated from moderately malignant (MCF7) and highly malignant (MDA-MB-231) human breast cancer cells exposed to valproic acid (VPA), a known epigenetic modifier drug involved in histone hyperacetylation and DNA demethylation. Due to chromosomal structural intricacy and preparative and technical limitations of analytical tools, we employed a label-free atomic force microscopy approach for simultaneously visualizing and mapping single chromosome elasticity and stretching modulus. Additionally, we performed electron transport characteristics through metaphase chromosomes to elucidate the effect of VPA. The chromosomal elasticity and electron transport alterations are manifestations of VPA-mediated chromatin's epigenetic changes. Our multiparametric strategy, as shown by receiver operating characteristics analyses with the physical properties of chromosomes, offers a new scope in terms of analytical tools for studying chromosomal structural changes/aberrations linked to cancer.

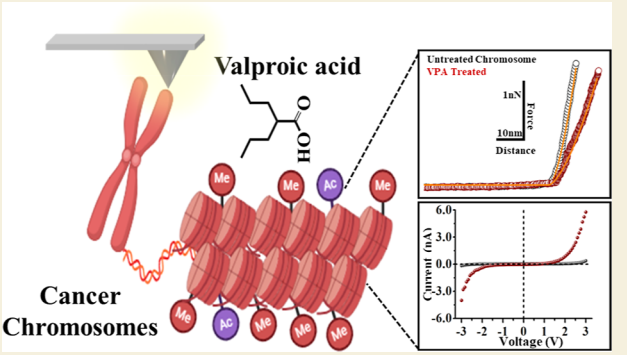

KEYWORDS: *chromosomes, breast cancer, valproic acid, atomic force microscopy, elasticity, electron transport*

INTRODUCTION

Breast cancer (BC) is the most common cancer diagnosed among women, with a 30% increase in the incidence rate over the last 20 years.[1] BC progression relies on genetic and epigenetic alterations; later, being reversible provides opportunities for therapeutic applications. Nucleic acid and peptide sequencing-based mass spectrometry (MS) is usually employed for mapping post-translational epigenetic modifications. Despite numerous efforts, the pathogenesis of BC is still unclear due to its biological heterogeneity, and effective therapeutic developments are challenging.[2] It is known that DNA methylation and histone post-translational modifications regulate gene expression without altering DNA sequence, which directly contributes to the tumorigenesis and progression of BC.[3] Hypermethylation of CpG islands of the gene promoter is catalyzed by a group of DNA methyltransferase enzymes (DNMTs, including DNMT1, DNMT2, and DNMT3) and is linked with transcriptional silencing of the concerned genes.[4] Modification of histones is controlled by a balance between histone acetyltransferase (HAT, which add an acetyl group to N-terminal lysine residues in histones) and histone deacetylase (HDAC) activities.[5,6] An imbalance between the two expressions leads to dynamic transitions in chromatin structure and is correlated to numerous cancers.[6] Several inhibitors of DNMTs and HDACs are approved by the US Food and Drug Administration (FDA) as anticancer drugs.[7] Valproic acid/sodium valproate (VPA) (2-propyl pentanoic acid, a low-molecular weight branched-chain fatty acid), is a FDA-approved drug for epilepsy, traditionally used as an anticonvulsant[8] (to prevent or treat seizures). This drug is also extensively reported to act on epigenetic dysregulations by inducing acetylation in histones and affecting the DNA methylation status in different cancers, including BC[8−14] (Scheme 1).

It is known that DNA methylation and histone acetylation modulate the chromatin structure. DNA methylation impacts

Received: October 22, 2024
Revised: January 15, 2025
Accepted: January 15, 2025
Published: February 12, 2025

https://doi.org/10.1021/jacsau.4c00991
JACS Au 2025, 5, 766−778

Scheme 1. Schematic Representation of the Epigenetic Modifications of DNA-Methylation and Histone Acetylation in Nucleosomes[a]

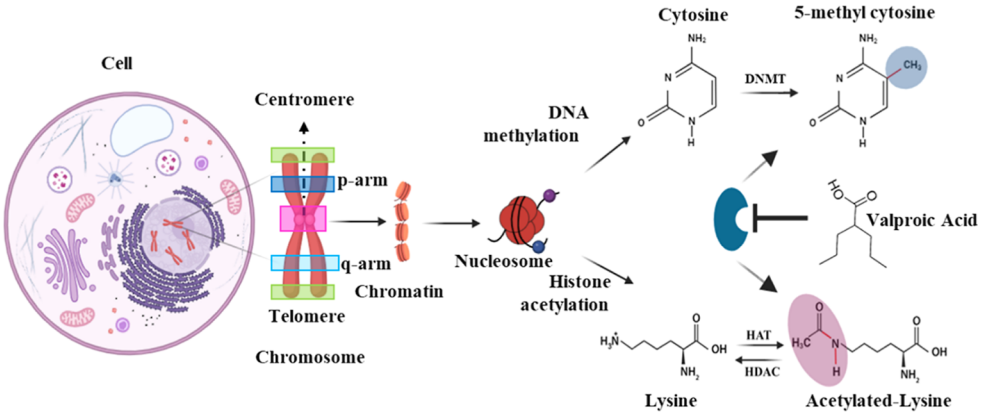

[a]VPA, a well-known HDAC and DNMT inhibitor.[14] DNA methyl transferase: DNMT, histone acetyl transferase: HAT, and histone deacetylase: HDAC.

chromatin compaction via linker DNA entry/exit angle alteration.[15] Similarly, acetylation modulates the interaction potential of the N-terminal tail domains of the core histones.[16] They both influence the folding and functional state of the chromatin fiber, which in turn modulates nucleosome accessibility to the transcription machinery.[12,16] Therefore, VPA induces chromatin structural rearrangements through epigenetic reprogramming involving demethylation and acetylation of specific genes/histones.[17] Previous biochemical studies revealed that VPA prompts chromatin decondensation, repair of damaged DNA, cell differentiation, apoptosis (by upregulation of Bak and downregulation of Bcl-2 expression), and cell cycle arrest (G1 or sub-G1 phases) in BC.[8,18] Presently, this compound is of great interest to the field and is undergoing many clinical trials for its antiproliferative properties in a variety of cancer types, including BC.[8] VPA is a known HDAC inhibitor that increases histone acetylation, particularly at lysine 9 of histone H3 and lysine 8 of histone H4, and can induce DNA demethylation, contributing to epigenetic reprogramming. These effects are crucial for altering chromatin structure and function, impacting chromosome elasticity, and electron transport. VPA mimics HDAC inhibition, leading to hyperacetylation of histones, which reduces their electrostatic affinity with DNA, resulting in a more open chromatin structure conducive to active transcription.[7] Notably, the acetylation of histone H3 at lysine 56 can influence DNA-histone interactions, enhancing chromosome elasticity and allowing easier deformation under mechanical stress.[8,9] VPA treatment also affects DNA methylation levels. The interplay between histone acetylation and DNA methylation varies by cell type, with VPA promoting demethylation through active and passive pathways. For example, in MCF7 cells, VPA-induced demethylation occurs passively, while in other cell types, it may involve ten-eleven translocation (TET) enzymes. Moreover, VPA decreases the expression of mRNA encoding SMC proteins and DNMT1, leading to significant chromatin structural changes and an increased sensitivity to nucleases. Studies show that DNA methylation can regulate gene expression by altering DNA's mechanical properties and its interactions with histones.[19] Interestingly, multiple studies have revealed a higher prevalence of chromosomal instability (CIN) in metastatic BC compared to primary BC.[20] This suggests a strong association between CIN and the process of metastasis. Therefore, it is crucial to understand that the mechanical properties of chromosomes are essential for their structural and functional integrity. We noticed that the physical properties of chromosomes and the effect of epigenetic modifiers (VPA and other drugs) on these properties were previously unexplored.

Observing single-chromosome morphology changes may be challenging due to the limitations of optical microscopy. Super-resolution optical microscopy is available in some cases;[21] notably, all these techniques require fluorescence staining, which depends on the affinity of the fluorescent dye with the chromatin and inadvertently affects its structure. We chose MCF7 (metastatic breast adenocarcinoma, estrogen receptor (ER)-positive) and MDA-MB-231 (epithelial adenocarcinoma, ER-negative, and highly tumorigenic and invasive[8,22]) for chromosome isolation, as model cell lines that have been used for many years by multiple groups.[23] Traditional southern hybridization technique revealed that MCF7 possesses the highest hypermethylation over other commonly studied BC cell lines.[24] Additionally, pattern analysis revealed that the overall methylation percentage in both cell lines is similar (~90% in MDA-MB-231 and ~93% in MCF7 cells).[24] Also, as per recent data, VPA significantly inhibits tumor progression in ER-positive and ER-negative[25] BC cell types than others.[18] In this work, we elucidated the physical outcome of VPA treatment on MCF7 and MDA-MB-231 chromosomes employing atomic force microscopy (AFM), a label-free single molecular detection technique capable of simultaneously providing nanoscale-resolved topography and elasticity maps (through AFM nanoindentation) at a precise location of a chromosome. The ability to study chromosomes *in situ* under physiological conditions in their pristine form is its major asset. With a conductive probe-AFM (CP-AFM), AFM is uniquely capable of measuring the electron flux through chromosomes with varying physical forces applied. This feature is useful in studying chromosomal structural rearrangements since cytosine methylation profoundly impacts DNA-mediated charge transport.[26] Only a handful of reports are available on AFM-based chromosomal biophysical dissections. Lipiec et al. applied AFM-Raman to reveal molecular alterations in HeLa chromosomes by inducing bleomycin,[27] previously they studied molecular differences between eu- and heterochromatin using AFM-IR based on differences in methylation status.[28]

https://doi.org/10.1021/jacsau.4c00991
JACS Au 2025, 5, 766−778

In another work, Lee's group evaluated the surface charge and stiffness of human B lymphocyte chromosomes by treating them with RNase and pepsin enzymes using KPFM and PF-QNM techniques.[29] In this study, for the first time, we quantified both the single chromosome elasticity and electron transport through isolated MCF7 and MDA-MB-231 single metaphase chromosomes using AFM to decipher the correlation between the chromatin structural alterations induced by VPA. This quantitative approach is valuable for assessing the disease progression, recognizing potential therapeutic responses, the efficiency of the drug treatment, and associated adverse effects, thereby offering critical insights for enhancing patient outcomes and altering individualized treatment strategies. The experimental setup is affordable and does not require special expertise to perform the required measurements and data analysis.

EXPERIMENTAL SECTION

Cell Culture and Metaphase Chromosome Isolation

MCF7 and MDA-MB-231 human BC cells (obtained from NCCS, Pune, India) were cultured in high glucose Dulbecco's modified Eagle medium (DMEM, Gibco) supplemented with 10% fetal bovine serum (FBS, Gibco) and 1% of antibiotics (streptomycin and penicillin, Gibco). Cells were incubated at 37 °C in a 5% CO_2 atmosphere. Metaphase chromosomes were isolated from MCF7 and MDA-MB-231 cells according to the protocol detailed elsewhere.[30] Briefly, 0.1 μg/mL colcemid (Sigma-Aldrich, USA) was added at 60−80% cell confluency and incubated overnight at 37 °C in a humidified atmosphere with 5% CO_2. Then, cells were detached from the culture flask using trypsin and neutralized with complete media. The cells were isolated by centrifugation at 1000 rpm for 5 min. After that, the excess supernatant was discarded. Next, prewarmed 0.075 M KCl (Sigma-Aldrich, USA) was added and mixed well, and the mixture was incubated for 20 min in a 37 °C water bath. Subsequently, 5 mL of freshly prepared cold fixative (methyl alcohol and acetic acid (Sigma-Aldrich, USA) were mixed 3:1, by volume/volume) was added to fix the cells. Then, the content was centrifuged, and the cell pellet was extracted. After washing the pellet with fixative, the chromosomal sample's concentration was checked by Nanodrop (Thermo Fisher). The chromosomes were treated with RNase (Sigma-Aldrich, R6513) and protease (Sigma-Aldrich, P6887) to remove nucleic acid and protein contaminants.[31] The sample was kept in the fixative solution at 4 °C for future use (maximum 24 h). We optimized the VPA concentration, incubated the cells with 0.1, 0.5, and 1 mM VPA (Sigma-Aldrich) dissolved in Milli-Q water for 24 h, isolated chromosomes, and performed IR spectroscopy. In optimized conditions, 1 mM VPA was incubated with cells for 24 h. Chromosomes were routinely checked under an optical and fluorescence microscope (Figure S1) (stained with acridine orange, Ti2E A1R MP, Nikon) before and after VPA treatment. Images were processed and quantified by using ImageJ software. We administered *in situ* VPA (1 μM) treatment to MCF-7 cell-derived chromosomes for 1 h to achieve reproducible changes in FT-IR spectroscopy results. We also checked for 0.1 and 0.5 μM concentrations with 30 min and 1 h incubation times (*in situ*).

Fourier-Transform Infrared Measurement

Fourier-transform infrared (FT-IR) spectra of chromosome samples were taken using the KBr window in a Nicolet iS20 FT-IR spectrometer (Thermo Fisher Scientific, Massachusetts, United States). The IR signal was measured with a deuterated triglycine sulfate (DTGS) detector. Each spectrum was an average of 64 scans in the range between 400 and 4000 cm^{-1}, with 4 cm^{-1} resolutions.

Principal Component Analysis

Here, spectral data for each chromosome sample were collected for a multivariate analysis. Baseline correction and vector normalization were achieved for each spectrum separately using Origin Lab (Northampton, MA). The first derivative was taken to minimize the baseline error and then smoothed by using the Savitzky−Golay method. Finally, principal component analysis (PCA) was performed using Origin software.

UV−Vis Measurement

The thermal stability of untreated and VPA-treated chromosomes was estimated by calculating the transition melting temperature (T_m) through a Cary 50 spectrophotometer with a stirred, temperature-controlled, single-cell Peltier accessory. The absorbance measurements were taken every 2.5 °C with a 5 min incubation at each temperature for equilibration.

Circular Dichroism Measurement

Circular dichroism (CD) spectra of chromosome samples were taken using a Jasco J-1500 CD spectrophotometer at 4 °C. The deconvolution of the CD signals into the relevant secondary structure was carried out by CDNN software, which was evaluated by using the BestSel CD deconvolution server.

Genomic DNA Samples

The genomic DNA samples were prepared using the DNeasy Blood and Tissue Kits for DNA isolation (Qiagen, Germany) to isolate genomic DNA from cells according to the manufacturer's protocol. We used a Nanodrop UV−vis spectrophotometer to determine the quantity of DNA obtained. The concentration of the DNA samples was ∼50 ng/μL for both.

Quantification of Global DNA Methylation by ELISA-Based Assay

The quantity of DNA methylation (% 5mC) was quantified using the MethylFlash Global DNA methylation (5-mC) ELISA Easy Kit (Colorimetric), following the manufacturer's instructions. Briefly, 100 ng of DNA samples was applied to an ELISA well strip. After DNA-surface binding, primary antibodies against 5-methyl cytosine were applied to an ELISA strip well. After color development, the absorbance was read at 450 nm using a BioTek, Synergy H1 microplate reader. The absolute quantity of global DNA methylation was determined using a standard curve.[32] The ELISA method yielded the degree of DNA methylation based on the OD value by

$$\%\ 5mC = [(\text{sample OD} - \text{negative OD})/(\text{slope} \times S)] \times 100$$

where, S is the amount of input sample DNA in ng.

AFM Imaging and Analysis

For AFM sample preparation, a freshly prepared chromosome sample (untreated and VPA-treated chromosomes) was placed on a cleaned glass slide/petri plate, incubated for 20 min, and washed briefly with PBS. Fluid imaging (in intermittent contact mode) and force spectroscopy were performed on an Asylum MFP-3D instrument (Asylum Research, Santa Barbara, USA) with a triangular silicon nitride probe (SNL-10, triangular A, spring constant 0.3 N/m) under PBS buffer (pH 7.4). All AFM images were analyzed using Igor Pro software.

AFM Nanoindentation

The chromosome spread was imaged in a PBS buffer in intermittent contact mode. Each chromosome and subchromosomal region were zoomed in and reimaged before starting force spectroscopy. The cantilever spring constant (SNL-10, triangular A, spring constant 0.1−0.3 N/m) and deflection sensitivity values were calibrated before each experiment. We carefully checked the height, length and width values of all parts of a single chromosome from fluid AFM images. The height values were always greater than 85 nm. A 500 × 500 nm area was selected on a single chromosome to generate force maps using a maximum applied force of 2 nN. Maximum 10−15 nm of indentation depths was made. The Young's modulus values were determined from the force maps using the Hertz model with spherical geometry having the equation[33] $\delta = [3(1 - \nu^2)/(4ER^{1/2})]^{2/3}F^{2/3}$. Here, δ, F, E, and R are the indentation, force, Young's modulus of the sample, and radius of the tip, respectively, and ν is the Poisson's ratio of the sample, which is assumed to be 0.3[34] using Igor Pro software.

https://doi.org/10.1021/jacsau.4c00991
JACS Au 2025, 5, 766−778

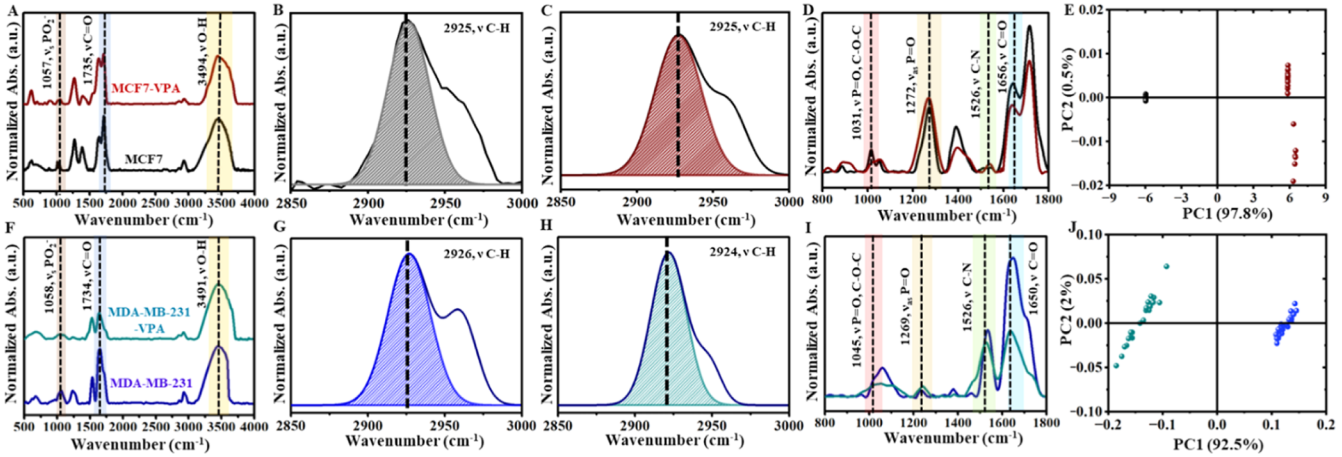

Figure 1. FT-IR average spectral profile of (A) MCF7 (black), MCF7-VPA-treated (wine), (F) MDA-MB-231 (blue), and MDA-MB-231-VPA-treated (cyan) chromosomes. Area under the curve (AUC) after Gaussian peak fitting for (B) MCF7, (C) MCF7-VPA-treated, (G) MDA-MB-231, and (H) MDA-MB-231-VPA-treated chromosomes, which represented the DNA-CH_3 band. Midinfrared spectral overlay of (D) MCF7 and (I) MDA-MB-231 and VPA-treated chromosomes represented different spectral signatures due to different methylation status in 800−1800 cm^{-1}. PCA score plot of both (E) MCF7 and (J) MDA-MB-231 chromosomes. Scores are based on the first two principal components: the region used for PCA was 400−4000 cm^{-1}.

Stretching Modulus

The single chromosome was mechanically contacted with an unmodified tip[35] by applying ∼100 pN contact force and retracted with ∼29.07 nm s^{-1} velocity. The force−separation curves were fitted with the worm-like chain (WLC) model using FODIS software[36] to extract the stretching modulus values of single chromosomes. According to this model, each unfolding event is described as $F(x) = K_BT/L_p\,[1/4\,(1 - x/L_c) - 2 + (x/L_c - 1/4)]$,[37] where F stands for force, x is the extension, K_B is the Boltzmann's constant, T is the temperature, L_p represents the persistence length, and L_c is the contour length of the domain. We varied the persistence length from 7 to 12 nm[38,39] to fit the force−separation profiles with the WLC model to calculate the contour lengths, through which the stretching modulus was calculated ($S = F_{st} \times L_c/\delta$), where S stands for stretching modulus, F_{st} is stretching force, δ is extension length, determined through the force−separations curves.[35,37,40] Regarding positioning accuracy in force volume measurements using AFM, we took several precautions to ensure precise and consistent data collection. We imaged entire chromosomes to obtain an overview of their shape and structure and measured the height and roughness values of the chromosomal regions. Following this, we systematically reduced the scan area to focus on smaller regions of the chromosome, reimaged every time, then remeasured the height values, carefully selected multiple points of interest that represent different sections of the chromosome body (centromere, telomere, p, and q arms), and collected force maps on each region of the chromosomes, which has allowed us to capture data from each chromosomal region and avoid positional bias from localized features or variations (the closed loop AFM scanner helps to maintain tip positioning).

Conductive Probe-AFM Analysis

An indium tin oxide (ITO)-coated glass substrate was thoroughly cleaned.[41] Freshly prepared chromosome solutions were deposited on a cleaned and dried ITO (1.0 cm^2) substrate, washed briefly with PBS, and dried with a weak stream of nitrogen gas. Each sample was imaged by intermittent-contact AFM (MFP-3D Asylum Research, Santa Barbara, USA), using AC240TS-R3 (Oxford Instruments, USA) to check the position of the chromosome spread. For $I-V$ measurements, a Pt−Ir-coated silicon cantilever (HQ-DPER-XSC11, MikroMasch, with a coated radius of 20 nm) was used. Potential sweeps were made from −3 to +3 V, and the resulting current responses were recorded (MFP-3D-ORCA mode). Each $I-V$ spectrum acquired on the single chromosome was the average of 4 sweeps. During each measurement, the force set point (10−100 nN) was calibrated and adjusted by applying a definite set point. All CP-AFM measurements were performed in ambient conditions where temperature and humidity were maintained at 24 ± 1 °C and 35−45%, respectively. 100 $I-V$ curves for both untreated (MCF7 and MDA-MB-231) and VPA-treated chromosomes and 5 μM, 72 h tetrathiomolybdate (TM)-treated MCF7 chromosomes at 10, 40, and 80 nN force loads were taken. The $I-V$ curves at different force loads were fitted with the Fowler−Nordheim (F−N) equation using Origin 8.5 software. We conducted CP-AFM experiments on three independently prepared samples. For each experiment, we measured at least ten different chromosomes in untreated and VPA-treated conditions (chromosomes were isolated from two cell lines). Similar to our strategy with force volume measurements, we imaged the entire chromosome first to obtain an overview of its structure and morphology. We then systematically focused on localized areas within the chromosome to perform CP-AFM analysis. We also routinely checked the CP-AFM tip coating by collecting force curves on bare ITO. We repeated the CP-AFM experiments on different chromosomes multiple times. Most data published in the field of CP-AFM (including biological samples and other inorganic materials) are collected in the air at a relative humidity of 30−60%. When measuring in ambient conditions, the presence of a water meniscus surrounding the tip/sample junction is unavoidable. However, we ensured that the metallic tip was touching the surface of the sample. We applied a force that was high enough to penetrate the water layer at the tip/sample junction (usually a few nanonewtons).[34] In this work, we performed all CP-AFM experiments at 50% RH and with a minimum of 10 nN force applied. The major limitation of CP-AFM is the tip-coating instability; we always performed CP-AFM experiments with new tips and repeated measurements to check the reproducibility. Previous studies have shown that chromosomes retain structural and mechanical properties under ambient conditions when examined over short time frames.[28,29] We ensured that all measurements were conducted rapidly to minimize potential environmental impacts. The chromosomes were also routinely checked through imaging. We ensured that the structural integrity remained intact during the measurements.

Overall, we measured 10 different chromosomes for each experimental case; each chromosome was assessed in 4 regions (centromere, telomere, p, and q arms), resulting in 60 chromosomes analyzed in the study. We performed VPA treatment *in situ* (total of 20 chromosomes) and in cells (40 chromosomes) and repeated experiments meticulously in MCF7 and MDA-MB-231 cell-derived chromosomes. At least 1000 curves with force volume maps were acquired for each chromosomal region to measure elasticity,

https://doi.org/10.1021/jacsau.4c00991
JACS Au 2025, 5, 766−778

Table 1. FT-IR Peak Assignments[9,28,30,46−50]

peak number	wavenumber (cm^{-1})					corresponding vibrational modes
	MCF7	MCF7-VPA	MCF7-VPA in situ	MDA-MB-231	MDA-MB-231 VPA	
1	644 (strong)	644 (weak)	644 (weak)	651 (strong)	652 (weak)	sugar−phosphate vibrations
2	1057	1057		1058		phosphate stretching
3	1031	1031	1031	1045	1045	P═O phospholipids stretching and C−O−C stretching
4	1272	1267	1267	1269	1270	C═O inorganic carbonate stretching and P═O asymmetric stretching
5	1389	1388	1388	1388	1388	antisymmetric aliphatic-CH deformation of methyl and methoxyl
6	1526	1526	1526	1527	1527	C−N amide group stretching
7	1656	1656 (weak)	1656 (weak)	1650	1650 (weak)	C═O amide group (cytosine)
8	1735	1735	1735	1734	1734	C═O stretching (carboxylic group)
9	2871 (weak)	2871 (strong)	2871 (strong)	2873 (weak)	2873 (strong)	C−H or CH_2 symmetric stretching vibrations
10	2925	2926	2923	2926	2924	CH_3 vibration or C−H− antisymmetric stretching vibrations
11	3494	3495	3495	3491	3490	O−H stretching/H-bonding

Table 2. Statistical Information for DNA-CH_3 Band Peak and Area Under the Curve Values for Both Untreated and VPA-Treated Chromosomes Obtained from FT-IR Spectral Profiles

chromosomes	peak starts (cm^{-1})	peak ends (cm^{-1})	area units	ratio control/treated	peak center (cm^{-1})
MCF7	2875	2975	0.37899	2.29	2925
MCF7-VPA	2870	2989	0.16548		2926
MDA-MB-231	2876	2991	0.36469	2.35	2926
MDA-MB-231 VPA	2882	2972	0.15518		2924

stretching modulus, and current values (4000 curves per chromosome).

ICP−MS Analysis

Freshly prepared chromosome solution was put in freshly prepared aqua regia (1:3 conc nitric acid and hydrochloric acid) and heated for 12 h at 60 °C for complete digestion and analyzed with a PerkinElmer inductively coupled plasma MS (ICP−MS).

ROC Analysis

Topography, force−distance, and *I-V* curves obtained on MCF7 and MDA-MB-231 chromosomes were analyzed to determine the volume, Young's modulus, stretching modulus, and current values, respectively. The receiver operating characteristic (ROC) curve was constructed using each input value (volume, Young's modulus, stretching modulus, and current response) between the MCF7 vs MCF-VPA and MDA-MB-231 vs MDA-MB-231-VPA individually using Origin 2023 software; p-value < 0.05 was considered statistically significant. A separability measure is the entire area under the ROC curve or AUC (area under the curve). A probability curve called the ROC is used to analyze test accuracy. It shows the extent to which the test is capable of class discrimination. A higher AUC makes it easier for the test to distinguish between individuals with medical conditions and those without. To produce the ROC curve, sensitivity is plotted on the y-axis, and 1-specificity is plotted on the x-axis. An excellent test is indicated by an AUC that is near 1, which indicates a good measure of separability. A test with an AUC near 0 is considered poor, as it has the lowest separability measure.[42]

RESULTS AND DISCUSSION

Biophysical and Biochemical Investigations on VPA-Treated MCF7 and MDA-MB-231 Chromosomes

The research involving various BC cell lines revealed that cellular response to VPA treatment depends on cell type, drug dosage, and incubation time.[8,11] Studies have reported IC_{50} values for VPA in MCF7 and MDA-MB-231 cells ranging from 800 μM to 2 mM, with higher concentrations resulting in extensive cell death and inflammatory responses.[18,43−45] Before isolating chromosomes, we incubated MCF7 and MDA-MB-231 cells with VPA (1 mM for 24 h). We tested for 0.1, 0.5, and 2 mM concentrations with 24 and 48 h incubation times. We determined that a 1 mM concentration and 24 h incubation time were optimal for observing significant differences in FT-IR spectra consistent with earlier reports.[9,13,14a] We attempted IR spectroscopy for untreated and VPA-treated MCF7 and MDA-MB-231 chromosome samples (Figure 1 and Table 1). We assigned the 2850−3050 cm^{-1} spectral range to the symmetric and asymmetric stretching of $-CH_2$, $-CH_3$, and C−H vibrations in 5-methylcytosine.[13] We observed an increase in absorbance intensity for untreated MCF7/MDB-MD-231 chromosomes compared to treated samples. The band centers were found at ∼2925 cm^{-1} for untreated chromosomes and ∼2923 cm^{-1} for VPA-treated chromosomes. The peak area for untreated chromosomes was approximately ∼2.3 times higher than that for VPA-treated chromosomes, suggesting reduced absorbed energy and changes in the chemical environment linked to lower DNA methylation levels in VPA-treated chromosomes (Table 2 and Figure 1B,C,G,H). The spectral range between 1610−1695 cm^{-1} was of Amide I (predominantly C═O stretching) of histone and C═O stretching, out-of-plane $-NH_2$ bending, dT, dG, dC, C/G/T, C═C stretching, and in-plane $-NH_2$ bending of DNA, which is highly informative of the changes in α-helices and β-sheet conformations that was affected by the VPA interactions. The changes in the intensity of peaks (∼1656 cm^{-1}) in this region represented the histone modifications, including hyperacetylation[13] (Table 1). For the peak ∼1270 cm^{-1} (nucleobases and $-PO_2$ antisymmetric stretching of the DNA), the absorption intensity of untreated was lower than VPA-treated chromosomes due to a higher abundance of cytosine methylation.[13] The spectral range

https://doi.org/10.1021/jacsau.4c00991
JACS Au 2025, 5, 766−778

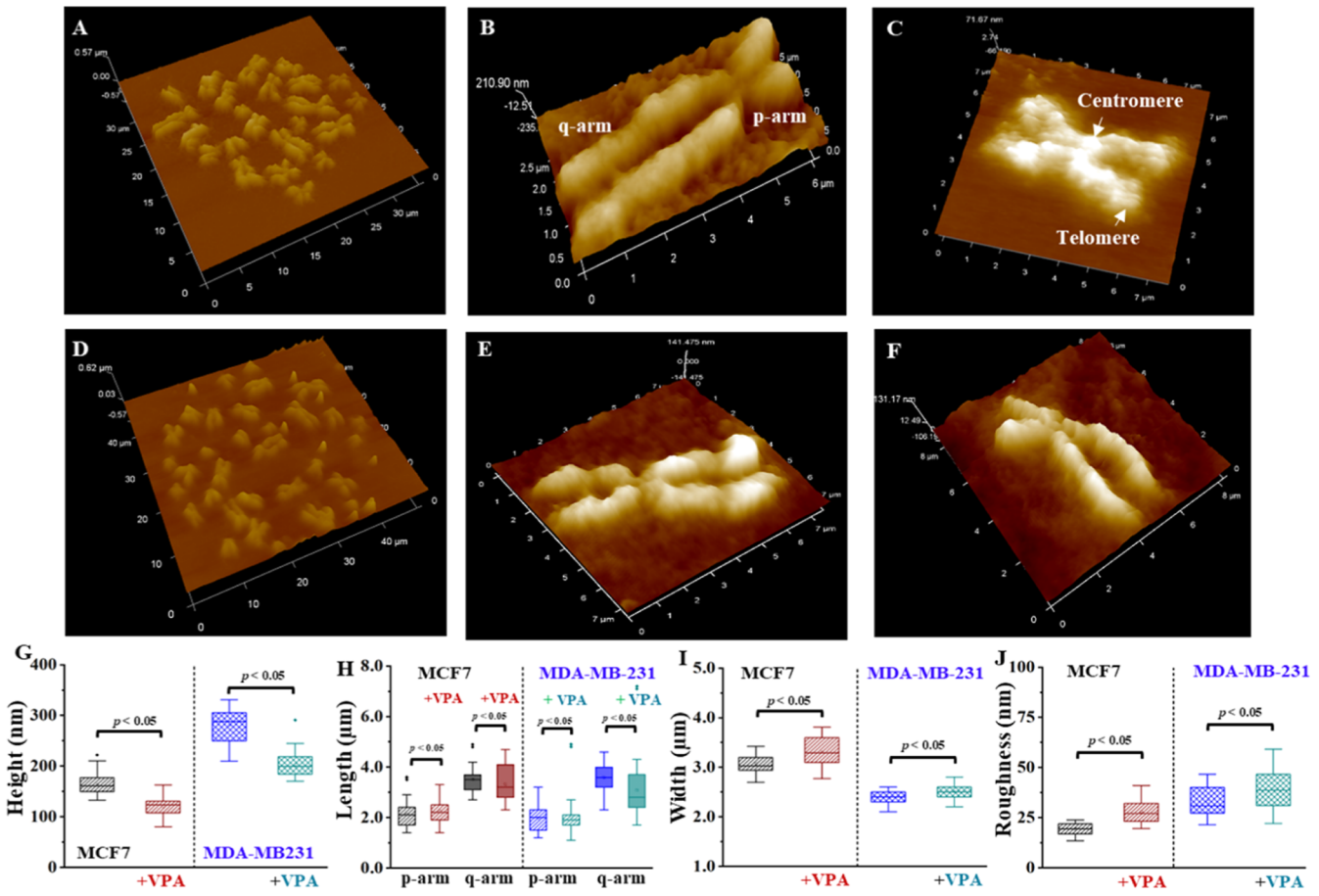

Figure 2. AFM 3D-topographic analysis of the (A–C) untreated and (D–F) VPA-treated MCF7 chromosomes in buffer. Box plots of (G) height and (H) length, (I) width, and (J) surface roughness (R_a) values of untreated and VPA-treated chromosomes (p values from unpaired t-test or ANOVA are shown).

1200–1300 cm^{-1} represented the amide III region, where higher intensities were observed for VPA-treated chromosomes, signifying loosely packaged chromatin[9,13,27,30] (Figure 1D,I). Next, we performed PCA (400–4000 cm^{-1}), which displayed the distinctions between untreated and VPA-treated chromosomes (Figure 1E,J). The overall analysis from FT-IR spectra and PCA deciphered that VPA treatment of chromosomes was successful (Tables 1 and 2).

Further, we performed UV melting experiments, where the melting curves of both chromosome samples showed the transition temperatures as ∼60 and ∼50 °C (T_m monitored at 260 nm) for untreated and VPA-treated MCF7 chromosome samples, respectively. The hypermethylated MCF7 sample had a melting temperature ∼10 °C higher than the treated sample[30] (Figure S3A). CD spectroscopy revealed higher α-helix and β-sheet contents and a decrease in turns, which are related to histone hyperacetylation induced by VPA treatment[51] (Figure S3B,C). Therefore, UV and CD experiments correlated well with the FT-IR findings. For biochemical validation, we performed ELISA using a global DNA methylation kit. The result indicates the % of global DNA methylation was 18.1 versus 12.6% for untreated and VPA-treated (1 mM for 24 h) MCF-7 DNA, respectively[32] (Figure S2). Collectively, biophysical (spectroscopy) and biochemical (ELISA) experiments univocally supported the VPA-induced DNA demethylation and histone hyperacetylation.

AFM Nanoindentation-Based Mechanical Characteristics of Chromosomes

We visualized MCF7 and MDA-MB-231 chromosomes with high-resolution AFM imaging in intermittent contact mode under physiological buffer conditions (Figures 2A–C and S5). Ultrastructural components of the centromere and telomere were frequently discerned (Figure 2C). We routinely checked the chromosome preparation with light and fluorescence microscopy before AFM imaging (Figure S1). We visualized chromosomes isolated from 1 mM VPA-treated cells for 24 h (Figures 2D–F and S5B) and compared the height, length, width and roughness values of both untreated (MCF7 and MDA-MB-231) and VPA-treated chromosomes (Figure 2G–J). All the measured values significantly changed before and after VPA treatment (Figure 2G–J), and these observations are linked to VPA-induced structural alterations in treated chromosomes (Tables S1 and S2). Interestingly, we found that while there was a reduction in the height of VPA-treated chromosomes compared to that of untreated, their width increased. This increase in width upon VPA treatment suggested that the chromosomes underwent structural relaxation, leading to a broader/flatter profile. The decrease in height could reflect chromatin decondensation due to VPA-induced epigenetic changes.

Next, AFM nanoindentation force spectroscopy was employed under physiological buffer conditions to measure the elasticity of a single chromosome. The AFM nano-

https://doi.org/10.1021/jacsau.4c00991
JACS Au 2025, 5, 766–778

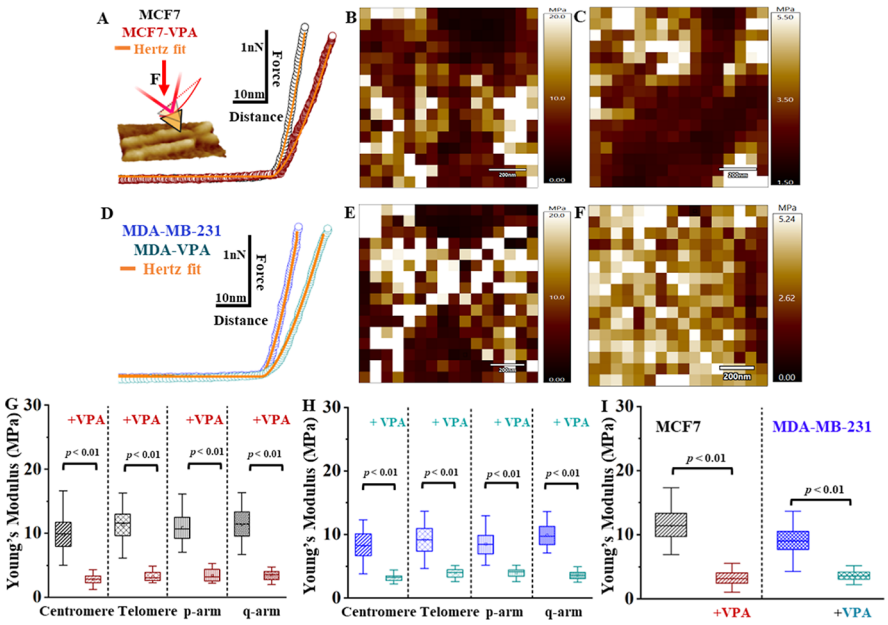

Figure 3. Representative force−distance profile of AFM nanoindentation on a single chromosome, (A) MCF7 (black) and MCF7-VPA-treated (wine), and (D) MDA-MB-231 (blue) and MDA-VPA-treated, fitted with Hertz model (orange) with spherical indenter geometry, and 3D AFM topographic view of a chromosome on a glass slide under buffer (inset). Force maps of Young's modulus for (B) MCF7, (C) MCF7-VPA, (E) MDA-MB-231, and (F) MDA-MB-231-VPA-treated chromosome at the centromere. Box plots of Young's modulus (using Hertz model) values of (G) MCF7 (black) and VPA-treated (wine), and (H) MDA-MB-231(blue) and VPA-treated (cyan) chromosomes at different chromosomal regions. (I) Average Young's modulus of untreated (MCF7, n = 10 and MDA-MB-231, n = 10) and VPA-treated chromosomes (n = 10 each; considering all four regions), p-values were calculated by one-way ANOVA, followed by the Tukey posthoc test.

Scheme 2. Condensed Chromatin Transformed to its Open Conformation upon VPA Treatment

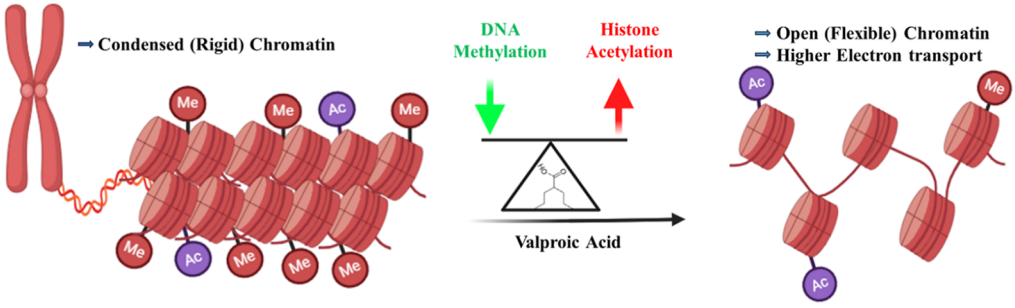

indentation mode provided a force−distance curve expressing the force exerted (max 2 nN) on a single chromosome by the AFM tip as the tip indented (max 20 nm; the indentation depth was not more than 10% of the chromosome height in buffer) the chromosome. Young's modulus was obtained by fitting the approach curve with the Hertz model (spherical indenter geometry) for both cases (Figure 3A,D).[34] We found that the VPA-treated chromosomes were strikingly more elastic than untreated chromosomes in both cells (12.5 ± 2 MPa (MCF7) vs 3.2 ± 0.4 (VPA-treated), $p < 0.01$) and (9.1 ± 2 MPa (MDA-MB-231) vs 3.7 ± 0.5 (VPA-treated), $p < 0.01$) (Figure 3B−J). This trend of elasticity was consistent with *in situ* data (Figure S6 and Table S1). The range of Young's modulus values of chromosomes was consistent with previous reports.[29,52] This data reveal how epigenetic reprogramming impacts the material properties of chromosomes.

DNA methylation adds a methyl group to cytosine DNA bases (Scheme 1), decreasing the repulsion between DNA strands, resulting in a more compact chromatin structure.[53] Earlier reports suggested that DNA demethylation can open up chromatin and prevent the strands from becoming tangled and also plays important roles in reinforcing the DNA during cell division, preventing DNA damage, and regulating gene expression and DNA replication.[54] In the case of hyperacetylation of histones, it relaxes the chromatin structure by adding negatively charged acetyl groups to specific lysine residues in histone (Scheme 1). This decreases the electrostatic affinity between histone proteins and DNA, which disrupts their interactions. The result is a more relaxed chromatin structure, which is associated with greater levels of gene transcription. Histone hyperacetylations are critical to various cellular processes, including nucleosome assembly, chromatin folding, and DNA damage repair.[55,56] Therefore, VPA transformed the condensed chromatin to its relaxed form (Scheme 2). We rigorously captured AFM force-volume maps at different subchromosomal regions (centromere, telomere, p, and q-arms) for mapping elasticity (Figure 3H,G) to investigate the effect of VPA on it. We found that VPA-treated chromosomes were uniformly elastic in 4 chromosomal regions compared to untreated ones (Table S2 and Figure 3I). The average height and Young's moduli of different subchromosomal regions (centromere, telomere, p, and q-

https://doi.org/10.1021/jacsau.4c00991
JACS Au 2025, 5, 766−778

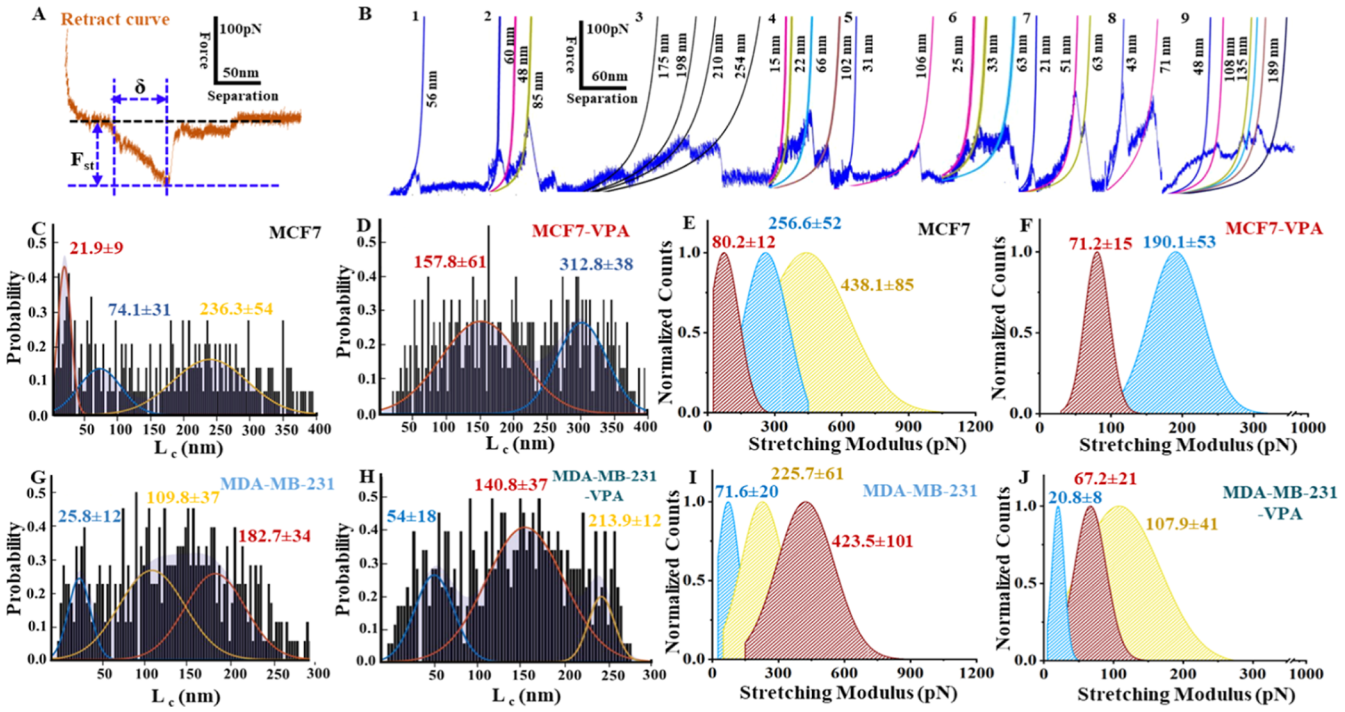

Figure 4. (A) Typical retract curve showing chromatin stretching (F_{st} = stretching force); the dotted black line represents the baseline. (B) Sample retract curves for single (1) (MCF7) and multiple rupture events (2,4: MCF7, 3,5: MCF7-VPA-treated, 6,8: MDA-MB-231, and 7,9: MDA-MB-231-VPA-treated), corresponding L_cs were quantified by WLC fitting. Multi-Gaussian fit (C) MCF7 (red, blue, and yellow lines), (D) MCF7-VPA (red and blue lines), (G) MDA-MB-231 (blue, yellow, and red lines), and MDA-MB-231-VPA (blue, red, and yellow lines) predicted the mean L_c ± SD. Corresponding stretching modulus (S) values were obtained for (E) MCF7 and (F) MCF7-VPA-treated and (I) MDA-MB-231 and (J) MDA-MB-231-VPA-treated chromosomes. Stretching modulus was calculated using $S = F_{st} \times L_c/\delta$ from force−separation curves (n = 25 curves for each case).[41]

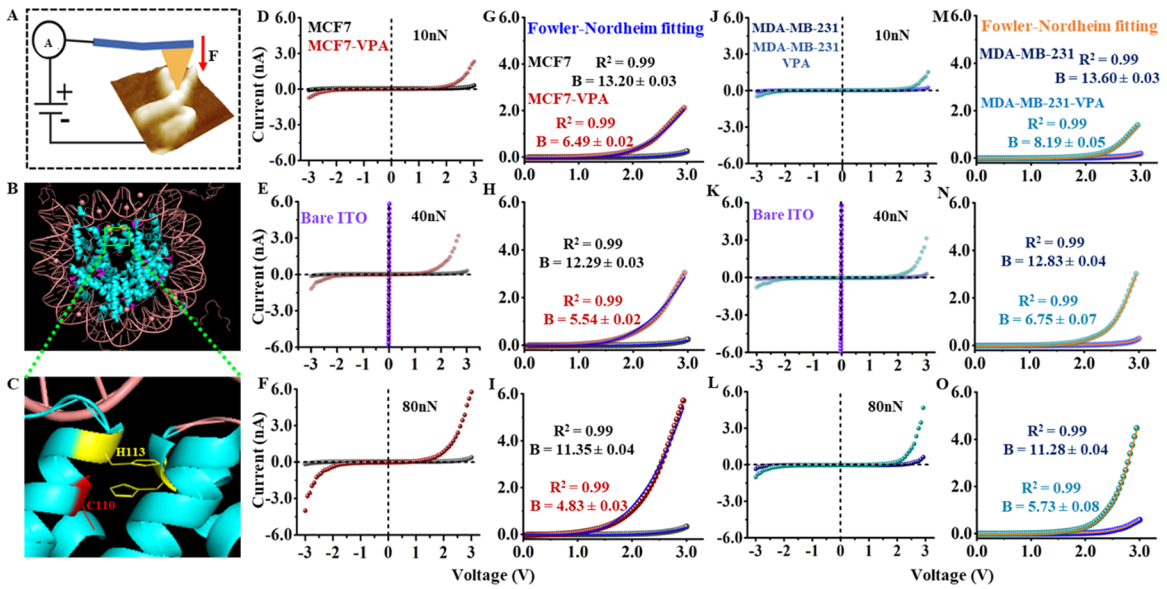

Figure 5. (A) Schematic illustration of junction configuration employed in the ETp measurement via single chromosome on an ITO substrate and (B) nucleosome core particle structure (Protein Data Bank (PDB) 1KX5). Box represents the H3−H3′ interface. (C) Interface residues H3H113 (histidine) and H3C110 (cysteine) are shown.[59] Overlay of I−V responses for bare ITO (blue), untreated (D−F) MCF7, and (J−L) MDA-MB-231, and VPA-treated chromosomes over the bias range of ±3.0 V (tip-positive). Applied forces were 10, 40, and 80 nN. (G−I,M−O) I−V curves of untreated and VPA-treated chromosomes were fitted with Fowler−Nordheim (F−N) model of the form $I(V) = AV^2 \exp(-B/V)$ for obtaining the respective "B " values.[60,63]

arms) are represented in Tables S2. We performed control experiments using DMSO and Acridine Orange (0.1%) added to chromosomes. The results showed no significant differences in chromosome elasticity between MCF7 cells treated with DMSO or Acridine Orange vs untreated, confirming that the observed effects are specific to VPA treatment (Figure S7A,B). We also measured Young's moduli of chromosomes on different substrates (plastic petri plates and glass slides). The

https://doi.org/10.1021/jacsau.4c00991
JACS Au 2025, 5, 766−778

measurements were consistent across both substrates (Figure S7C), concluding that the substrate-stiffening effect did not significantly impact our measurements.

We next quantified the stretching modulus (S) from the chromosome samples, which measures the resistance of chromosomes to deformation under mechanical stress, indicating how easily the chromatin fiber can be stretched. Stretching of the chromosomes at a characteristic tip−substrate separation was measured and fitted with a WLC model while fitting both persistence length (L_p) and the contour length (L_c) were set as adjustable parameters. Stretching modulus was calculated using this equation $S = F_{st} \times L_c/\delta$, where F_{st}: stretching force and δ: extension length (Figure 4A). L_p values were consistent with the previous reports.[38,39,57] Most of these curves showed multiple interaction signatures (Figure 4B, 2−9), while a few represented a single interaction event (Figure 4B 1); the nonspecific interaction curves were excluded. The contour length increased upon VPA treatment in both cases (Figure 4C,D,G,H); we observed a few distributions of contour lengths in each case. The highest L_c for MCF7 chromosomes was 236.3 ± 54 vs 312.8 ± 38 nm for VPA-treated, while for MDA-MB-231 was 182.7 ± 34 vs 213.9 ± 12 nm for VPA-treated (Figure 4C,D,G,H). A higher contour length in VPA-treated chromosomes represented the end-to-end length of the chromosome in a fully stretched condition, suggesting a more relaxed or flexible chromatin fiber. We then calculated the corresponding stretching modulus (S) values for both cases (438.1 ± 85 (MCF7) vs 190.1 ± 53pN (VPA-treated)) and (423.5 ± 101 (MDA-MB-231) vs 107.9 ± 41pN (VPA-treated)) (Figure 4E,F,I,J). A lower stretching modulus in VPA-treated chromosomes indicated a similar trend of increased chromatin flexibility and relaxation, consistent with VPA's role as an epigenetic modifier drug.

CP-AFM Study to Assess Electron Transport through Chromosomes

We performed CP-AFM analysis to quantify electron transport through untreated and treated single chromosomes. In CP-AFM, the probe physically touches the biomolecule; the tip positioning is decoupled from the sample conductivity, allowing more precise knowledge of the relative positions of the tip and sample in the vertical plane.[58] Electron transport characteristics of biological macromolecules can be assessed with carefully maintained varying applied forces[58] (Figure 5A). Freshly prepared chromosome samples were deposited on ITO substrates for CP-AFM, and current−voltage ($I-V$) curves were captured under ambient conditions. The $I-V$ characteristics of both untreated (MCF7 and MDA-MB-231) and VPA-treated chromosome samples were captured at ±3 V applied bias with 10, 40, and 80 nN forces.[b] The experiments were repeated for *in situ* administration of VPA to chromosomes (Figure S8). Chromosomes are supramolecular complexes of DNA and proteins. They were conductive due to the presence of DNA, proteins,[31,52] and cupric ions bound to H3−H3′ interface of the histone tetramer[59] (Figure 5B,C). The measured conductivity was comparable to metalloproteins.[60] We quantified cupric ions with ICP−MS measurements, and 4 × 10^4 ppb copper was found to be associated with one preparation of MCF7 chromosomes where we started with approximately 10^6 cells.

At all of the applied forces, VPA-treated chromosomes were more conductive than untreated samples, and the current values were significantly higher than those of untreated chromosomes (Figures 5D−F,J−L, and S6, S8). With increasing applied forces from 10 to 80 nN, the current values increased for both samples. We found that our measured $I-V$ curves could be well fit with F−N tunneling model of the form, $I(V) = AV^2 \exp(-B/V)$.[60] This model was applied only when the barrier height between the underlying ITO substrate and chromosomes was low. According to the F−N equation, the higher the conductivity, the lower the B value (details of B value calculation[60]). To calculate the corresponding "B" values, the positive side of the curves was used, as the CP-AFM tip was positive relative to the substrate (Figure 5G−I,M−O). Under all forces, the B values for untreated chromosomes were higher than those for VPA-treated chromosomes in both cases. Therefore, electron transport was facilitated more in VPA-treated chromosomes than in untreated ones. We have also measured the electron transport in different chromosomal regions of untreated and VPA-treated MCF7 chromosomes (10−80 nN applied force) (Figures S9 and S10). Additionally, to evaluate the significance of cupric ions present intrinsically in the chromosomes, we treated the MCF7 chromosomes with TM, an oral copper-chelating drug.[61] TM efficiently depletes intracellular copper in BC cells and in vivo mouse models.[62,63] We treated the MCF7 cells with 5 μM TM for 72 h. We quantified the decrease in the cupric ions with ICP−MS measurements (4 × 10^4 vs 1.23 × 10^4 ppb) and performed the CP-AFM experiment (Figure S11). We observed a significant decrease in the current values (Figure S11A−C). Additionally, we quantified the zinc (2.1 × 10^2 ppb), magnesium (3.6 × 10^2 ppb), and calcium (1.4 × 10^4 ppb) in MCF-7 chromosomes using ICP−MS. The intrinsic cupric ions and other metal ions in the chromosome samples plausibly contributed to higher electron transport through them. With VPA treatment, the chromosomes were relaxed, which helped the AFM probe reach out to the deeply buried cupric/other ions. We also found a correlation between the extent of chromosome relaxation and current values observed at certain bias voltages (Figure S10, S12) (beyond 2 V), but no such discrimination could be made at the lower voltages. We propose that the copper and other metal ions that reside deeper inside the chromosomes can be accessed only at higher voltages.[34] Also, the electron transport capacity could be increased with a higher amount of force applied (compression) (Figure 5). This could be due to the compression of the histone polypeptide part, enhancing DNA-histone interactions since such compression effectively could reduce the atom-to-atom distances and increase the electron transport rate through chromosomes.[58]

It is well reported that the methyl group impacts the DNA duplex stability and charge transport pathways.[64] Tao et al. observed a significant change in conductance upon methyl modification on cytosine. The destabilization due to cytosine methylation led to an increased HOMO−LUMO gap, which ultimately affected the electron transport characteristics of methylated DNA.[26,30,65] Earlier reports also suggested that electron transfer is highly facilitated from histone protein to DNA (thymine bases) in irradiated damaged chromatin.[66] In our study, epigenetic alterations resulted in an open relaxed chromatin (Scheme 2) that highly impacted DNA-histone interactions, provided better accessibility to cupric/other metal ions, and significantly enhanced the conductivity of the VPA-treated chromosomes, especially at higher applied forces.

VPA induces chromatin decondensation, primarily through increased histone acetylation and DNA demethylation, which

https://doi.org/10.1021/jacsau.4c00991
JACS Au 2025, 5, 766−778

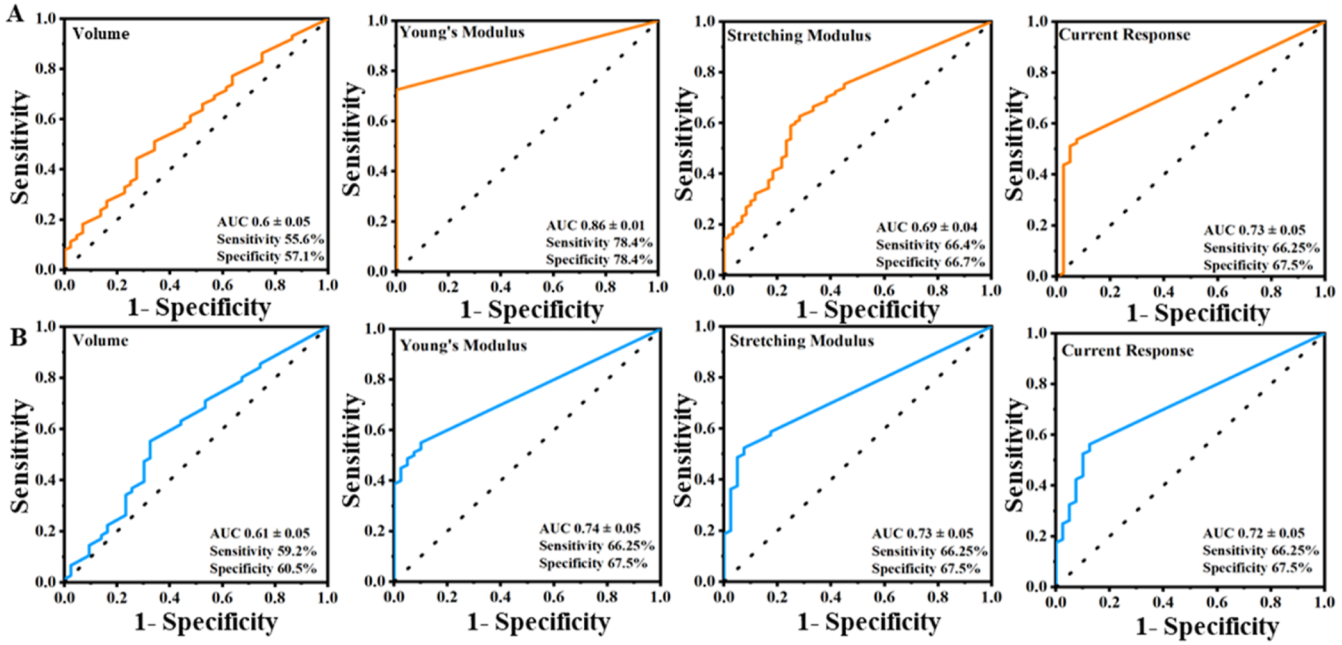

Figure 6. ROC analysis showing the discriminative efficacy of the volume, Young's modulus, stretching modulus, and current response of the chromosomes (A) MCF7 and MCF-7-VPA-treated and (B) MDA-MB-231 and MDA-MB-231-VPA-treated. Area under the ROC curve (AUC) of different groups is mentioned (volume, Young's modulus, stretch modulus, and current response, respectively) (n = 10 each case). Standard deviation, 95% confidence interval, p value, sensitivity, and specificity values were shown (Table S3).

reduces chromatin rigidity (Scheme 2).[19,26] Unlike earlier studies focusing mainly on biochemical aspects with a few reports on the IR spectroscopy of chromatin decondensation through epigenetic modifications, our work further correlates these epigenetic changes with chromosome physical properties. This work uniquely offers a detailed analysis of how VPA influences chromosome compaction and stiffness, directly impacting chromosome mechanics. We performed label-free AFM measurements on elasticity, stretching modulus, and electron transport, providing quantitative insights into how VPA-mediated alterations impact the structural integrity of chromosomes. This correlation between chromosomal epigenetic modifications and biophysical properties has been largely unexplored in previous studies. Additionally, we introduced the electron transport properties of chromosomes, which correlate well with their mechanical behavior. Advanced AFM-based biophysical techniques to study epigenetic modifications in chromosomes to elucidate physical property changes have previously been unreported.

Next, to tease out the discriminatory efficiency of using AFM-based assays, we further employed ROC analysis to evaluate volume, Young's modulus, stretching modulus, and current responses of the untreated and treated chromosomes. Topography images, force distance, and IV curves obtained on chromosomes were analyzed to determine the respective values. The ROC curve was constructed using each input value between the untreated (MCF7 and MDA-MB-231) and VPA-treated chromosomes individually with Origin 2023 software; p-value < 0.05 was considered statistically significant. A separability measure is the entire area under the ROC curve or AUC. A probability curve called the ROC is used to analyze test accuracy. It shows the extent to which the test is capable of class discrimination. A higher AUC makes it easier for the test to distinguish between individuals with medical conditions and those without.[42,67] After careful feature selection, we tested our constructed model using the ROC curve (Figure 6A,B). All four AFM-derived parameters had high sensitivity and specificity in distinguishing untreated and treated chromosomes (Table S3 and Figure 6). These results indicated the capability of the AFM-based topography, nanomechanical, and electron transport properties of the chromosomes in evaluating drug treatment efficacy.[42] This also aligns with the growing emphasis on personalized medicine, where therapeutic regimens are tailored based on an individual's cancer's molecular and structural characteristics. The significant structural changes in chromosomes following VPA/other epigenetic modifier drug treatment suggest that chromosomal mechanics could serve as biomarkers for treatment efficacy and pave the way for the development of new therapeutic strategies to restore chromosomal stability in cancer cells. This strategy can be extrapolated for early disease diagnostics, routine therapy outcome, disease recurrence, etc. The major limitations of AFM-based strategies include sample preparation steps, extended testing times, low throughput, unsuitability for in vivo application, etc.

Unlike other biophysical techniques, AFM offers several advantages for studying epigenetic-cancer-related chromosomal alterations: AFM operates label-free, unlike fluorescence-based imaging, and can image samples under physiological conditions, preserving the native chromatin structure. This provides detailed 3D topographical data. AFM can provide high-resolution images, mechanical properties, and electron transport assessments in a single experiment. This offers unique advantages compared to techniques such as magnetic/optical tweezers. While techniques such as bisulfite sequencing, ChIP-seq, and cryo-EM offer high specificity and resolution, they are highly expensive, resource-intensive, and time-consuming. In contrast, AFM experiments on patient-derived cancer cell chromosomes could be relatively convenient, less costly, and more reproducible. Overall, AFM's label-free, high-

https://doi.org/10.1021/jacsau.4c00991
JACS Au 2025, 5, 766−778

resolution, and multiplex capabilities make it a promising tool for studying epigenetic changes in cancer.

CONCLUSIONS

VPA induced the demethylation of DNA and hyperacetylation of histones; both factors together transformed the undulant condensed MCF7 and MDA-MB-231 chromatin to its relaxed form. The chromosomal structural alterations resulted in increased resilience and pliability and electron transport capabilities of VPA-treated chromosomes. CIN has a substantial impact on the growth and advancement of cancer. A multitude of variables can induce abnormalities in chromosomes, including epigenetic dysregulation. Chromosomes have inherent mechanical qualities that are crucial for their optimal functioning. Changes in these mechanical properties can significantly impact the stability and functioning of chromosomes. Therefore, the mechanical data of cancer chromosomes has many implications on how the cancer therapeutic drugs work at the chromatin level, mainly because it could help assess CIN in different subparts of the chromosomes in the future. AFM offers a few important advantages in studying chromosomes and their biophysical properties, but it has a few limitations. The huge numbers of chromosomes in a cancer cell are tedious to study with AFM. The mechanical/electrical properties of chromosomes may vary with the same cells with different passage numbers and culturing conditions. Therefore, the future goal of our lab will be to study clinical samples (patient's blood) to validate our AFM-based approach. We hope to apply multiparametric AFM and statistical (ROC, multivariate) analysis together to reveal the intrinsic crosstalk between CIN and structural aberrations and functional outcomes. The bioelectronic aspects of chromosomes are also emerging; tumor-treating fields (TTF) combined with chemotherapeutic drugs are increasingly used for treating aggressive brain tumors, and a few clinical trials are undergoing. TTF is a cancer treatment that uses alternating electric fields to disrupt the ability of some types of tumor cells to grow and spread by targeting proteins in cancer cells that are essential to cell division. The CP-AFM-based-chromosomal electron flux data holds insight into how chemotherapy drugs combined with TTF[68] could be manipulated for better therapeutic outcomes in aggressive cancers. Chromosome-based bioelectronics for medical device applications could be another exciting pathway for future applications.

ASSOCIATED CONTENT

Supporting Information

The Supporting Information is available free of charge at https://pubs.acs.org/doi/10.1021/jacsau.4c00991.

Optical and fluorescence microscopy images of chromosomes, ELISA, CD and UV study, in situ FT-IR, AFM topographic and nanoindention, additional CP-AFM study, and ROC details (PDF)

AUTHOR INFORMATION

Corresponding Author

Tatini Rakshit − *Department of Chemistry, Shiv Nadar Institution of Eminence, Delhi-NCR, Uttar Pradesh 201314, India;* orcid.org/0000-0002-4182-9240; Email: tatini.rakshit@snu.edu.in

Authors

Tanya Agrawal − *Department of Chemistry, Shiv Nadar Institution of Eminence, Delhi-NCR, Uttar Pradesh 201314, India;* orcid.org/0009-0009-4618-0717

Debashish Paul − *Department of Chemistry, Shiv Nadar Institution of Eminence, Delhi-NCR, Uttar Pradesh 201314, India;* orcid.org/0000-0002-6764-5052

Amita Mishra − *Department of Chemistry, Shiv Nadar Institution of Eminence, Delhi-NCR, Uttar Pradesh 201314, India*

Ganesan Arunkumar − *Department of Cell Biology and Physiology, School of Medicine, University of New Mexico, Albuquerque, New Mexico 87131, United States*

Complete contact information is available at: https://pubs.acs.org/10.1021/jacsau.4c00991

Author Contributions

Methodology, validation, formal analysis, data interpretation, investigation, writing−original draft, and visualization: T. A., D. P., and A. M. Conceptualization, data interpretation, writing, and editing: T.R. and G.A. Conceptualization, methodology, writing and editing, supervision, project administration, and funding acquisition: T.R. CRediT: **Tanya Agrawal** data curation, formal analysis, writing - original draft; **Debashish Paul** data curation, formal analysis; **Amita Mishra** data curation, formal analysis; **Ganesan Arunkumar** methodology, writing - review & editing; **Tatini Rakshit** conceptualization, funding acquisition, investigation, methodology, project administration, resources, software, supervision, validation, visualization, writing - review & editing.

Notes

The authors declare no competing financial interest.

ACKNOWLEDGMENTS

T.A. and D.P. thank Shiv Nadar University and CSIR-HRDG (123-2639-898/2K23/1) for SRF fellowships, respectively. T.R. thanks DST/INSPIRE/04/2017/002375, SERB (CRG/2019/007013 and CRG/2023/003029), and Shiv Nadar University, Delhi NCR, for funding and research facilities, including MFP-3D AFM.

ADDITIONAL NOTES

[a]We also treated VPA on chromosomes *in situ*. The drug treatment to chromosomes *in situ* method allows for targeted application, minimizing systemic exposure and potential side effects. This approach generally requires lower drug doses than *in vivo* treatments, which still provide insights into the drug's effects. We administered *in situ* VPA (1 μM) treatment to MCF7 cell-derived chromosomes for 1 h to achieve reproducible changes in FT-IR spectroscopy results (Figure S4). We also checked for 0.1 and 0.5 μM concentrations with 30 min and 1 h incubation times (*in situ*). We determined that 1 μM concentration and 1 h incubation time were optimal for observing significant differences for *in situ* administration.
[b]We performed CP-AFM experiments for in situ added VPA to MCF7 chromosomes and the data were highly consistent with the cell-VPA-treated data (Figure S8).

REFERENCES

(1) Bray, F.; Ferlay, J.; Soerjomataram, I.; Siegel, R. L.; Torre, L. A.; Jemal, A. Global Cancer Statistics 2018: GLOBOCAN Estimates of

Incidence and Mortality Worldwide for 36 Cancers in 185 Countries *CA. Ca-Cancer J. Clin.* **2018**, *68* (6), 394−424.
(2) Janni, W. Targeted Therapy of Breast Cancer. *Oncol. Res. Treat.* **2016**, *39* (3), 100−101.
(3) Li, W.; Wu, H.; Sui, S.; Wang, Q.; Xu, S.; Pang, D. Targeting Histone Modifications in Breast Cancer: A Precise Weapon on the Way. *Front. Cell Dev. Biol.* **2021**, *9*, 1−33.
(4) Sharma, S.; Kelly, T. K.; Jones, P. A. Epigenetics in Cancer. *Carcinogenesis* **2010**, *31* (1), 27−36.
(5) Gallinari, P.; Marco, S. D.; Jones, P.; Pallaoro, M.; Steinkühler, C. HDACs, Histone Deacetylation and Gene Transcription: From Molecular Biology to Cancer Therapeutics. *Cell Res.* **2007**, *17* (3), 195−211.
(6) Wawruszak, A.; Kalafut, J.; Okon, E.; Czapinski, J.; Halasa, M.; Przybyszewska, A.; Miziak, P.; Okla, K.; Rivero-Muller, A.; Stepulak, A. Histone Deacetylase Inhibitors and Phenotypical Transformation of Cancer Cells. *Cancers* **2019**, *11* (2), 148−231.
(7) Cai, F. F.; Kohler, C.; Zhang, B.; Wang, M. H.; Chen, W. J.; Zhong, X. Y. Epigenetic Therapy for Breast Cancer. *Int. J. Mol. Sci.* **2011**, *12* (7), 4465−4476.
(8) Wawruszak, A.; Halasa, M.; Okon, E.; Kukula-Koch, W.; Stepulak, A. Valproic Acid and Breast Cancer: State of the Art in 2021. *Cancers* **2021**, *13* (14), 3409−3423.
(9) Mello, M. L. S. Sodium Valproate-Induced Chromatin Remodeling. *Front. Cell Dev. Biol.* **2021**, *9*, 1−7.
(10) Cheng, Y.; He, C.; Wang, M.; Ma, X.; Mo, F.; Yang, S.; Han, J.; Wei, X. Targeting Epigenetic Regulators for Cancer Therapy: Mechanisms and Advances in Clinical Trials. *Signal Transduction Targeted Ther.* **2019**, *4* (1), 62.
(11) Wawruszak, A.; Luszczki, J. J.; Grabarska, A.; Gumbarewicz, E.; Dmoszynska-Graniczka, M.; Polberg, K.; Stepulak, A. Assessment of Interactions between Cisplatin and Two Histone Deacetylase Inhibitors in MCF7, T47D and MDA-MB-231 Human Breast Cancer Cell Lines - An Isobolographic Analysis. *PLoS One* **2015**, *10* (11), No. e0143013.
(12) Milutinovic, S.; D'Alessio, A. C.; Detich, N.; Szyf, M. Valproate Induces Widespread Epigenetic Reprogramming Which Involves Demethylation of Specific Genes. *Carcinogenesis* **2007**, *28* (3), 560−571.
(13) Veronezi, G. M. B.; Felisbino, M. B.; Gatti, M. S. V.; Mello, M. L. S.; Vidal, B. d. C. DNA Methylation Changes in Valproic Acid-Treated HeLa Cells as Assessed by Image Analysis, Immunofluorescence and Vibrational Microspectroscopy. *PLoS One* **2017**, *12* (1), 01707400.
(14) de Campos Vidal, B.; Mello, M. L. S. Sodium Valproate (VPA) Interactions with DNA and Histones. *Int. J. Biol. Macromol.* **2020**, *163*, 219−231.
(15) Jimenez-useche, I.; Yuan, C. The Effect of DNA CpG Methylation on the Dynamic Conformation of a Nucleosome. *Biophys. J.* **2012**, *103* (12), 2502−2512.
(16) Eberharter, A.; Becker, P. B. Histone Acetylation: A Switch between Repressive and Permissive Chromatin. Second in Review on Chromatin Dynamics. *EMBO Rep.* **2002**, *3* (3), 224−229.
(17) Sanaei, M.; Kavoosi, F. The Effect of Valproic Acid on Intrinsic, Extrinsic, and JAK/STAT Pathways in Neuroblastoma and Glioblastoma Cell Lines. *Res. Pharm. Sci.* **2022**, *17* (4), 392−409.
(18) Giordano, F.; Paoli, A.; Forastiero, M.; Marsico, S.; De Amicis, F.; Marrelli, M.; Naimo, G. D.; Mauro, L.; Panno, M. L. Valproic Acid Inhibits Cell Growth in Both MCF-7 and MDA-MB231 Cells by Triggering Different Responses in a Cell Type-Specific Manner. *J. Transl. Med.* **2023**, *21* (1), 165−214.
(19) Severin, P. M. D.; Zou, X.; Gaub, H. E.; Schulten, K. Cytosine Methylation Alters DNA Mechanical Properties. *Nucleic Acids Res.* **2011**, *39* (20), 8740−8751.
(20) Liao, Y. Y.; Cao, W. M. The Progress in Our Understanding of CIN in Breast Cancer Research. *Front. Oncol.* **2023**, *13*, 1−7.
(21) Pujals, S.; Albertazzi, L. Super-Resolution Microscopy for Nanomedicine Research. *ACS Nano* **2019**, *13* (9), 9707−9712.
(22) Gong, Y.; Liu, Y. R.; Ji, P.; Hu, X.; Shao, Z. M. Impact of Molecular Subtypes on Metastatic Breast Cancer Patients: A SEER Population-Based Study. *Sci. Rep.* **2017**, *7*, 45411−45510.
(23) Comşa, Ş.; Cîmpean, A. M.; Raica, M. The Story of MCF-7 Breast Cancer Cell Line: 40 Years of Experience in Research. *Anticancer Res.* **2015**, *35* (6), 3147−3154.
(24) Huang, T. H. M.; Perry, M. R.; Laux, D. E. Methylation Profiling of CpG Islands in Human Breast Cancer Cells. *Hum. Mol. Genet.* **1999**, *8* (3), 459−470.
(25) Li, G. F.; Qian, T. L.; Li, G. S.; Yang, C. X.; Qin, M.; Huang, J.; Sun, M.; Han, Y. Q. Sodium Valproate Inhibits MDA-MB-231 Breast Cancer Cell Migration by Upregulating NM23H1 Expression. *Genet. Mol. Res.* **2012**, *11* (1), 77−86.
(26) Hihath, J.; Guo, S.; Zhang, P.; Tao, N. Effects of Cytosine Methylation on DNA Charge Transport. *J. Phys.: Condens. Matter* **2012**, *24* (16), 164204−164211.
(27) Urbańska, M.; Sofińska, K.; Czaja, M.; Szymoński, K.; Skirlińska-Nosek, K.; Seweryn, S.; Lupa, D.; Szymoński, M.; Lipiec, E. Molecular Alterations in Metaphase Chromosomes Induced by Bleomycin. *Spectrochim. Acta, Part A* **2024**, *312*, 124026.
(28) Lipiec, E.; Ruggeri, F. S.; Benadiba, C.; Borkowska, A. M.; Kobierski, J. D.; Miszczyk, J.; Wood, B. R.; Deacon, G. B.; Kulik, A.; Dietler, G.; Kwiatek, W. M. Infrared Nanospectroscopic Mapping of a Single Metaphase Chromosome. *Nucleic Acids Res.* **2019**, *47* (18), e108−e115.
(29) Roh, S.; Lee, T.; Cheong, D. Y.; Kim, Y.; Oh, S.; Lee, G. Direct Observation of Surface Charge and Stiffness of Human Metaphase Chromosomes. *Nanoscale Adv.* **2023**, *5* (2), 368−377.
(30) Agrawal, T.; Paul, D.; Saroj, S.; Ali, A.; Choubey, V.; Mukherjee, D.; Pal, S.; Rakshit, T. Label-Free Physical-Analytical Techniques Reveal Epigenetic Modifications of Breast Cancer Chromosomes. *J. Phys. Chem. B* **2023**, *127* (15), 3534−3542.
(31) Tamayo, J.; Miles, M. Human Chromosome Structure Studied by Scanning Force Microscopy after an Enzymatic Digestion of the Covering Cell Material. *Ultramicroscopy* **2000**, *82* (1−4), 245−251.
(32) Cheon, H.; Paik, J. H.; Choi, M.; Yang, H. J.; Son, J. H. Detection and Manipulation of Methylation in Blood Cancer DNA Using Terahertz Radiation. *Sci. Rep.* **2019**, *9* (1), 6413−6510.
(33) Butt, H. J.; Cappella, B.; Kappl, M. Force Measurements with the Atomic Force Microscope: Technique, Interpretation and Applications. *Surf. Sci. Rep.* **2005**, *59* (1−6), 1−152.
(34) Rakshit, T.; Banerjee, S.; Mishra, S.; Mukhopadhyay, R. Nanoscale Mechano-Electronic Behavior of a Metalloprotein as a Variable of Metal Content. *Langmuir* **2013**, *29* (40), 12511−12519.
(35) Clausen-Schaumann, H.; Rief, M.; Tolksdorf, C.; Gaub, H. E. Mechanical Stability of Single DNA Molecules. *Biophys. J.* **2000**, *78* (4), 1997−2007.
(36) Galvanetto, N.; Perissinotto, A.; Pedroni, A.; Torre, V. Fodis: Software for Protein Unfolding Analysis. *Biophys. J.* **2018**, *114* (6), 1264−1266.
(37) Janshoff, A.; Neitzert, M.; Oberdörfer, Y.; Fuchs, H. Force Spectroscopy of Molecular Systems - Single Molecule Spectroscopy of Polymers and Biomolecules. *Angew. Chem., Int. Ed.* **2000**, *39* (18), 3212−3237.
(38) Manning, G. S. The Persistence Length of DNA Is Reached from the Persistence Length of Its Null Isomer through an Internal Electrostatic Stretching Force. *Biophys. J.* **2006**, *91* (10), 3607−3616.
(39) Jun, S.; Herrick, J.; Bensimon, A.; Bechhoefer, J. Persistence Length of Chromatin Determines Origin Spacing in Xenopus Early-Embryo DNA Replication: Quantitative Comparisons between Theory and Experiment. *Cell Cycle* **2004**, *3* (2), 211−217.
(40) Koh, K. D.; Chiu, H. C.; Riedo, E.; Storici, F. Measuring the elasticity of ribonucleotide (s)-containing DNA molecules using AFM. *RNA Nanotechnology and Therapeutics: Methods and Protocols*; Springer, 2015; Vol. *1297*, pp 43−57.
(41) Xia, N.; Gerhardt, R. A. Fabrication and Characterization of Highly Transparent and Conductive Indium Tin Oxide Films Made with Different Solution-Based Methods. *Mater. Res. Express* **2016**, *3* (11), 116408−116412.

https://doi.org/10.1021/jacsau.4c00991
JACS Au 2025, 5, 766−778

(42) Kumar, R.; Indrayan, A. Receiver operating characteristic (ROC) curve for medical researchers. *Indian Pediatr.* **2011**, *48* (4), 277−287.
(43) Fortunati, N.; Bertino, S.; Costantino, L.; Bosco, O.; Vercellinatto, I.; Catalano, M. G.; Boccuzzi, G. Valproic Acid Is a Selective Antiproliferative Agent in Estrogen-Sensitive Breast Cancer Cells. *Cancer Lett.* **2008**, *259* (2), 156−164.
(44) Hodges-Gallagher, L.; Valentine, C. D.; Bader, S. E.; Kushner, P. J. Inhibition of Histone Deacetylase Enhances the Anti-Proliferative Action of Antiestrogens on Breast Cancer Cells and Blocks Tamoxifen-Induced Proliferation of Uterine Cells. *Breast Cancer Res. Treat.* **2007**, *105* (3), 297−309.
(45) Olsen, C. M.; Meussen-Elholm, E. T. M.; Røste, L. S.; Taubøll, E. Antiepileptic Drugs Inhibit Cell Growth in the Human Breast Cancer Cell Line MCF7. *Mol. Cell. Endocrinol.* **2004**, *213* (2), 173−179.
(46) Banyay, M.; Gra, A. Structural Effects of Cytosine Methylation on DNA Sugar Pucker Studied by FTIR. *J. Mol. Biol.* **2002**, *324* (2), 667−676.
(47) Banyay, M.; Sarkar, M.; Graslund, A. A Library of IR Bands of Nucleic Acids in Solution. *Biophys. Chem.* **2003**, *104* (2), 477−488.
(48) Kelly, J. G.; Najand, G. M.; Martin, F. L. Characterisation of DNA Methylation Status Using Spectroscopy (Mid-IR versus Raman) with Multivariate Analysis. *J. Biophotonics* **2011**, *4* (5), 345−354.
(49) Vidal, B. d. C.; Ghiraldini, F. G.; Mello, M. L. S. Changes in Liver Cell DNA Methylation Status in Diabetic Mice Affect Its FT-IR Characteristics. *PLoS One* **2014**, *9* (7), 1022955.
(50) Mello, M. L. S.; Vidal, B. C. Analysis of the DNA Fourier Transform-Infrared Microspectroscopic Signature Using an All-Reflecting Objective. *Micron* **2014**, *61*, 49−52.
(51) Feng, Y.; Wang, J.; Asher, S.; Hoang, L.; Guardiani, C.; Ivanov, I.; Zheng, Y. G. Histone H4 Acetylation Differentially Modulates Arginine Methylation by an in Cis Mechanism. *J. Biol. Chem.* **2011**, *286* (23), 20323−20334.
(52) Wang, B.; Yang, F.; Dong, J.; Li, J.; Wang, Y.; Qu, K.; Wei, H.; Wang, Z. Analysis of the Mechanical Properties of Chromosomes in Air and Liquid by AFM. *IEEE International Conference on Manipulation, Manufacturing and Measurement on the Nanoscale (3M-NANO)*, 2021; pp 43−46.
(53) Choy, J. S.; Wei, S.; Lee, J. Y.; Tan, S.; Chu, S.; Lee, T. H. DNA Methylation Increases Nucleosome Compaction and Rigidity. *J. Am. Chem. Soc.* **2010**, *132* (6), 1782−1783.
(54) Zhou, T.; Yang, L.; Lu, Y.; Dror, I.; Dantas Machado, A. C.; Ghane, T.; Di Felice, R.; Rohs, R. DNAshape: A Method for the High-Throughput Prediction of DNA Structural Features on a Genomic Scale. *Nucleic Acids Res.* **2013**, *41*, 56−62.
(55) Gujral, P.; Mahajan, V.; Lissaman, A. C.; Ponnampalam, A. P. Histone Acetylation and the Role of Histone Deacetylases in Normal Cyclic Endometrium. *Reprod. Biol. Endocrinol.* **2020**, *18* (1), 84.
(56) Bannister, A. J.; Kouzarides, T. Regulation of Chromatin by Histone Modifications. *Cell Res.* **2011**, *21* (3), 381−395.
(57) Zaichuk, T.; Marko, J. F. Single-Molecule Micromanipulation Studies of Methylated DNA. *Biophys. J.* **2021**, *120* (11), 2148−2155.
(58) Rakshit, T.; Bera, S.; Kolay, J.; Mukhopadhyay, R. Nanoscale Solid-State Electron Transport via Ferritin: Implications in Molecular Bioelectronics. *Nano-Struct. Nano-Objects* **2020**, *24*, 100582−100610.
(59) Attar, N.; Campos, O. A.; Vogelauer, M.; Cheng, C.; Xue, Y.; Schmollinger, S.; Salwinski, L.; Mallipeddi, N. V.; Boone, B. A.; Yen, L.; Yang, S.; Zikovich, S.; Dardine, J.; Carey, M. F.; Merchant, S. S.; Kurdistani, S. K. The Histone H3-H4 Tetramer Is a Copper Reductase Enzyme. *Science* **2020**, *369* (6499), 59−64.
(60) Rakshit, T.; Mukhopadhyay, R. Solid-State Electron Transport in Mn-, Co-, Holo-, and Cu-Ferritins: Force-Induced Modulation Is Inversely Linked to the Protein Conductivity. *J. Colloid Interface Sci.* **2012**, *388* (1), 282−292.
(61) Weiss, K. H.; Askari, F. K.; Czlonkowska, A.; Ferenci, P.; Bronstein, J. M.; Bega, D.; Ala, A.; Nicholl, D.; Flint, S.; Olsson, L.; Plitz, T.; Bjartmar, C.; Schilsky, M. L. Bis-Choline Tetrathiomolybdate in Patients with Wilson's Disease: An Open-Label, Multicentre, Phase 2 Study. *Lancet Gastroenterol. Hepatol.* **2017**, *2* (12), 869−876.
(62) Cui, L.; Gouw, A. M.; LaGory, E. L.; Guo, S.; Attarwala, N.; Tang, Y.; Qi, J.; Chen, Y. S.; Gao, Z.; Casey, K. M.; Bazhin, A. A.; Chen, M.; Hu, L.; Xie, J.; Fang, M.; Zhang, C.; Zhu, Q.; Wang, Z.; Giaccia, A. J.; Gambhir, S. S.; Zhu, W.; Felsher, D. W.; Pegram, M. D.; Goun, E. A.; Le, A.; Rao, J. Mitochondrial Copper Depletion Suppresses Triple-Negative Breast Cancer in Mice. *Nat. Biotechnol.* **2021**, *39* (3), 357−367.
(63) Liu, Y. L.; Bager, C. L.; Willumsen, N.; Ramchandani, D.; Kornhauser, N.; Ling, L.; Cobham, M.; Andreopoulou, E.; Cigler, T.; Moore, A.; LaPolla, D.; Fitzpatrick, V.; Ward, M.; Warren, J. D.; Fischbach, C.; Mittal, V.; Vahdat, L. T. Tetrathiomolybdate (TM)-Associated Copper Depletion Influences Collagen Remodeling and Immune Response in the Pre-Metastatic Niche of Breast Cancer. *npj Breast Cancer* **2021**, *7* (1), 108−111.
(64) Rauch, C.; Trieb, M.; Wellenzohn, B.; Loferer, M.; Voegele, A.; Wibowo, F. R.; Liedl, K. R. C5-Methylation of Cytosine in B-DNA Thermodynamically and Kinetically Stabilizes BI. *J. Am. Chem. Soc.* **2003**, *125* (49), 14990−14991.
(65) Tian, Y.; Liu, Z.; Cheng, Y.; Liu, H. Electronic Properties for Detection of DNA Methylation. *J. Phys.:Conf. Ser.* **2019**, *1324* (1), 012052−012057.
(66) Cullis, P. M.; Jones, G. D.; Symons, M. C.; Lea, J. S. Electron transfer from protein to DNA in irradiated chromatin. *Nature* **1987**, *330*, 773−774.
(67) Safari, S.; Baratloo, A.; Elfil, M.; Negida, A. Evidence Based Emergency Medicine; Part 5 Receiver Operating Curve and Area under the Curve. *Emergency* **2016**, *4* (2), 111−113.
(68) Kirson, E. D.; Dbalý, V.; Tovaryš, F.; Vymazal, J.; Soustiel, J. F.; Itzhaki, A.; Mordechovich, D.; Steinberg-Shapira, S.; Gurvich, Z.; Schneiderman, R.; Wasserman, Y.; Salzberg, M.; Ryffel, B.; Goldsher, D.; Dekel, E.; Palti, Y. Alternating Electric Fields Arrest Cell Proliferation in Animal Tumor Models and Human Brain Tumors. *Proc. Natl. Acad. Sci. U.S.A.* **2007**, *104* (24), 10152−10157.

https://doi.org/10.1021/jacsau.4c00991
JACS Au 2025, 5, 766−778